This is a non-peer reviewed preprint submitted to EarthArXiV. This paper has been submitted to Geochemical Perspective Letters

Enhanced Petrogenic Organic Carbon Oxidation during the Paleocene-Eocene Thermal Maximum

Emily H. Hollingsworth[1]*, Robert B. Sparkes[2], Jean M. Self-Trail[3], Gavin L. Foster[1], and Gordon N. Inglis[1]

[1] School of Ocean and Earth Science, University of Southampton, Southampton, UK

[2] Department of Natural Sciences, Manchester Metropolitan University, Manchester, UK

[3] U.S. Geological Survey, Florence Bascom Geoscience Center, Reston, VA, USA

*****Corresponding author: Emily H. Hollingsworth

Email: e.hollingsworth@soton.ac.uk

Abstract

The Paleocene-Eocene Thermal Maximum (PETM) was a transient global warming event associated with rapid inputs of carbon into the ocean-atmosphere system. The oxidation of petrogenic organic carbon (OC_{petro}) may have acted as a positive feedback mechanism that helped prolong the PETM. However, there are few proxies that can estimate OC_{petro} oxidation in the geological past. Previous studies have applied Raman spectroscopy to reveal spatial variability in OC_{petro} oxidation within modern systems. Here, we use this approach to assess the extent of OC_{petro} oxidation during the PETM. Data from the mid-Atlantic Coastal Plain exhibits a shift from disordered to highly graphitised OC_{petro} following the onset of the PETM, which coincides with an increase in the input of thermally mature biomarkers. This suggests enhanced oxidation of OC_{petro}, indicating an additional source of CO_2 within the PETM. Our work highlights the utility of Raman spectroscopy as a novel tool to constrain OC_{petro} oxidation during the PETM and other climatic events throughout Earth's history.

1. Introduction

At the Paleocene-Eocene boundary, an abrupt carbon cycle perturbation gave rise to a global warming event (~4–6°C; Tierney *et al.,* 2022) known as the Paleocene-Eocene Thermal Maximum (PETM; ~56 Ma). The initial flux of carbon into the ocean-atmosphere system occurred within ~3–21 kyrs (the onset of the PETM; see Kirtland Turner, 2018 and references therein), yet the PETM persisted for a further 170 ± 30 kyrs (the "body" of the PETM; Zeebe & Lourens, 2019). The long duration of the PETM can only be explained by additional carbon inputs, however the sources are still debated. Proposed mechanisms include the slow dissociation of oceanic methane hydrates (*e.g.,* Zeebe, 2013), oxidation of terrestrial organic carbon (*e.g.,* Bowen, 2013), and/or pulsed releases of carbon from hydrothermal vent complexes (see Jin *et al.,* 2024 and references therein).

Recent work suggests that CO_2 emitted from the oxidation of "petrogenic" organic carbon (OC_{petro}) could partly explain the body of the PETM (Lyons *et al.,* 2019; Hollingsworth *et al.,* 2024). OC_{petro} is comprised of thermally mature organic matter (*e.g.,* shale, lignite, coal). During erosion and mobilisation, OC_{petro} could oxidise and release CO_2 back into the exogenic carbon pool. Throughout the PETM, the low-to-mid latitudes are associated with enhanced OC_{petro} delivery to the marine realm (Lyons *et al.,* 2019; Hollingsworth *et al.,* 2024). However, this is based on biomarker thermal maturity ratios that can only recognise OC_{petro} generated prior to metamorphism. At burial temperatures in excesss of <165 °C, diagnostic features of biomarkers are lost in a process known as metagenesis. As such, a new approach is needed to fingerprint OC_{petro} that formed at higher burial temperatures. In addition, calculating the subsequent CO_2 release requires identifying the fraction of OC_{petro} that oxidised during transport (*i.e.* the oxidation efficiency). This remains challenging to quantify in the geological record. Lyons et al. (2019) assumed a wide range (15–85%) based on present-day observations of less- and more-oxidising environments (*e.g.,* Bouchez *et al.,* 2010; Hilton *et al.,* 2014). The resulting global estimates of OC_{petro}-derived CO_2 during the body of the PETM span two orders-of-magnitude (10^2–10^4 PgC; Lyons *et al.,* 2019). Thus, to better quantify the role of this positive feedback mechanism as a CO_2 source in the past, OC_{petro} oxidation efficiencies must be constrained.

Raman spectroscopy can detect OC_{petro} that formed during metamorphism by characterising nm-scale differences in crystallinity. Amorphous (*i.e.* disordered carbon) to highly crystalline

(*i.e.* graphite) OC_{petro} corresponds with moderate (<350 °C) to high (350–650 °C) burial temperatures, respectively (Beyssac *et al.,* 2002). Since the porous structure of disordered carbon makes it more susceptible to oxidation, the distribution of disordered vs. graphitised OC_{petro} in marine deposits can also inform how much OC_{petro} was oxidised during transport from land-to-sea (*e.g.,* Galy *et al.,* 2008; Bouchez *et al.,* 2010). This approach has most commonly been utilised in modern systems but rarely to environments of the past. Here, we use Raman spectroscopy to characterise the type of OC_{petro} that was delivered to two contrasting PETM-aged shallow-marine sites. First, we validate the application of Raman spectroscopy as a tool to fingerprint OC_{petro} delivery in PETM-aged sediments. We then determine the extent of oxidation and thus the fate of OC_{petro} during the PETM.

2. Material and Methods

We investigate two contrasting PETM-aged shallow-marine sites. South Dover Bridge (**SDB**) exhibits little change in the source of organic carbon (Hollingsworth *et al.,* 2024), whereas the International Ocean Drilling Program Expedition 302 Site M0004A (**ACEX**) shows enhanced OC_{petro} delivery during the PETM (Lyons *et al.,* 2019). SDB core was drilled in the Salisbury Embayment of the mid-Atlantic Coastal Plain and ACEX core was drilled on the Lomonosov Ridge, Central Arctic Ocean (Fig. 1).

Raman spectroscopy is a non-destructive technique that can be used to assess the crystallinity of carbonaceous materials. We follow the methodology outlined in Sparkes et al. (2013), which was specifically developed to facilitate the analyses of sedimentary rocks. Overall, 36 samples from SDB and 12 samples from ACEX were processed and analysed with an InVia Raman spectrometer (Renishaw). Firstly, wet sediments were either freeze-dried or placed in a 50 ºC oven overnight (Table S-2). The samples were then ground to a fine powder with a Pulverisette 5 planetary mill (Fritsch), for 2 min at 300 rpm. The agate mill and balls were cleaned in between each sample with isopropanol. The homogenised samples were then compressed between two glass slides to create an area which can be rastered under a 50x magnification microscope. Using a 514 nm Ar-ion laser, all potential carbonaceous particles were examined by brief exposure (short acquisition; 2 seconds at 10 % power) and, if confirmed, spectra were produced from extended exposure (long acquisition; 60 seconds at 10 % power). To increase the chance that the data is representative of the population, 10 spectra were collected for each sample. The peaks in each spectrum were fitted using an updated script

(https://github.com/robertsparkes/raman-fitting/releases/tag/v1.1.5) of the automated process described in Sparkes et al. (2013), and manually checked for inconsistencies.

3. Results

In total, 360 spectra from SDB and 120 spectra from ACEX were collected. The automated process resulted in low residuals, and only 7 spectra from SDB and 1 spectrum from ACEX were excluded due to a noise-to-signal ratio greater than 1:3. In previous studies, spectra were characterised as either: (i) disordered carbon, (ii) intermediate carbon, (iii) mildly graphitised carbon, and (iv) highly graphitised carbon (Sparkes *et al.*, 2013). However, our data suggests a predominantly bimodal distribution between spectra that consists of a single sharp peak at 1580 cm^{-1} (G peak; Fig. 2a), signifying pure graphite, and spectra with a broader G peak alongside a peak at 1350 cm^{-1}, 1620 cm^{-1}, 1500 cm^{-1}, and 1200 cm^{-1} (D1–4; Fig. 2b). The latter indicates disordered carbon, as more peaks are introduced and widen with increasing disorder (Sparkes *et al.*, 2013). As such, the spectra were categorised into either graphitised carbon (*e.g.*, Fig. 2a) or disordered carbon (*e.g.*, Fig. 2b) (Table S-1 to S-2). This separation was based on peak burial temperatures, which were calibrated using the R2 and RA2 peak area ratio (see Sparkes *et al.*, 2013).

With only 10 spectra collected for each sample, the data was combined into key time intervals to minimise uncertainty. The time intervals are as follows: Pre-PETM, PETM (onset and body), Recovery, and Post-PETM (see Hollingsworth *et al.*, 2024 and references therein) (Table S-1 to S-2). At SDB, the Pre-onset excursion (POE) in the latest Paleocene (*i.e.* Pre-PETM) is also isolated using the definition from Babila et al. (2022). Time-series plots of SDB and ACEX can be found in the Supporting Information for more detailed examination of changes through time (Fig. S-1 and S-2). Overall, the two sites exhibit contrasting results. At ACEX, the abundance of disordered vs. graphitised carbon is relatively stable throughout the record (Fig. 3c). On the other hand, at SDB there is a 33% increase in the mean percentage of graphitised carbon from Pre-PETM (including the POE) to during the PETM (Fig. 3a). This is the largest change observed between the time intervals and is statistically highly significant (P <0.001). Intriguingly, the transition from dominantly disordered to graphitised carbon does not occur until ~1.5 m above the onset of the PETM (Table S-1 and Fig. S-1). At both SDB and ACEX, the Recovery and Post-PETM intervals show a higher percentage of graphitised carbon than in the Pre-PETM.

4. Discussion

4.1. Raman spectroscopy as a tool to fingerprint OC_{petro} delivery during the PETM

The utilisation of Raman spectroscopy to fingerprint OC_{petro} delivery is mostly restricted to studies on modern river catchments and continental shelf systems (*e.g.,* Galy *et al.,* 2008; Bouchez *et al.,* 2010; Sparkes *et al.,* 2018, 2020; Sun *et al.,* 2022). To validate its application in PETM-aged shallow-marine sediments, the results of this study are compared to published biomarker thermal maturity ratio data from the same cores (Lyons *et al.,* 2019; Hollingsworth *et al.,* 2024). Here, the C_{31} S/(S+R) ratio is plotted adjacent to the percentage of graphitised carbon for SDB (Fig. 3b) and ACEX (Fig. 3d). The S/(S + R) ratio corresponds to the early stages of the oil window and values closer to 0.6 indicate higher thermal maturity.

Overall, there are remarkable similarities between the proxies at both sites, with the records exhibiting little variability at ACEX (Fig. 3c,d) and large fluctuations at SDB (Fig. 3a,b). Notably, the temporal trends parallel each other at SDB, with an increase in the percentage of graphitised carbon and the C_{31} S/(S+R) ratio from Pre-PETM to the POE and PETM intervals. Both proxies also show that the latter shift lags the onset of the PETM by ~1.5 m, suggesting a delayed carbon cycle response (Fig. S-1). Furthermore, the high values remain in the recovery and do not fully return to Pre-PETM levels after the termination of the PETM. Our new data supports previous findings indicating no drastic changes in the organic carbon source at ACEX (Hollingsworth *et al.,* 2024) but enhanced OC_{petro} delivery at SDB (Lyons *et al.,* 2019) during the PETM. Collectively, this validates the application of Raman spectroscopy as another tool to fingerprint OC_{petro} delivery in PETM-aged sediments. This approach, when combined with biomarker analyses, has the advantage of expanding the type of OC_{petro} detected and the number of PETM-aged localities that can be investigated. Raman spectroscopy is particularly powerful in tracing allochthonous OC_{petro} at sites with extensive post-depositional diagenesis and metamorphism, as long as burial temperatures do not exceed >650 °C (Sparkes *et al.,* 2020).

4.2. Characterisation of OC_{petro} and their potential sources

At ACEX, the lack of graphitised carbon (Fig. 3c) and lower C_{31} S/(S+R) values (Fig. 3d) suggest input of relatively thermally immature organic carbon. This is consistent with the

delivery of well-preserved pollen and spores (Sluijs *et al.,* 2008). However, the occurrence of disordered carbon throughout (Fig. 3c) implies some contribution from OC_{petro}, such as a relatively thermally immature lignite. This is corroborated with the presence of biomarkers diagnostic of peats and/or lignite deposits (*e.g.,* C_{31} αβ hopanes; Hollingsworth *et al.,* 2024).

At SDB, the increase in graphitised carbon (Fig. 3a), thermally mature biomarkers (Fig. 3b), and a positive shift in the bulk organic carbon isotope ($\delta^{13}C_{org}$) record (Lyons *et al.,* 2019) indicates input of OC_{petro} during the PETM. Kopp et al. (2009), initially hypothesised that Cretaceous-aged upland deposits, such as the Potomac Group, could have been a source of sediment to the PETM Salisbury Embayment. Indeed, similarities were found with the biomarker thermal maturity ratios from the Raritan Formation of the upper Potomac Group and the PETM-aged SDB core (Lyons *et al.,* 2019). The $\delta^{13}C_{org}$ and source rock properties (*e.g.,* T_{max}) also exhibit comparable values (Lyons *et al.,* 2019). During the PETM, the correlation between the percentage of graphitised carbon (Fig. 3a) and the C_{31} S/(S+R) ratios (Fig. 3b) suggests that the graphitised OC_{petro} may have been sourced from the same stratigraphic sequence. In contrast, the decoupling of the two proxies during the POE could reflect multiple sources of OC_{petro}. However, a high abundance of graphitised carbon in the PETM interval implies high burial temperatures (350–650 °C; Beyssac *et al.,* 2002) that should severely diminish or completely destroy biomarkers. Therefore, the graphitised OC_{petro} was likely reworked into the Raritan Formation and subsequently re-exhumed alongside the thermally mature biomarkers during the PETM. This is consistent with present-day observations showing that graphite particles survive transport over thousands of kilometres (*e.g.,* Galy *et al.,* 2008) and persist over multiple erosion cycles (*e.g.,* Jehlicka & Rouzaud, 1990; Sparkes *et al.,* 2020).

4.3. Enhanced OC_{petro} oxidation in the mid-Atlantic Coastal Plain during the PETM

During the PETM, the mid-Atlantic Coastal Plain was characterised by intense precipitation events (see Carmichael *et al.,* 2017 and references therein), exacerbated erosion (*e.g.,* John *et al.,* 2008), and a ~20 fold increase in linear sedimentation rates (Lyons *et al.,* 2019). Evidence of terrigenous input (*e.g.,* charcoal, seed pods, fern spores; Self-Trail *et al.,* 2017) and pronounced freshwater runoff (*e.g.,* an abundance of dinoflagellates that thrive in brackish water with high turbidity; Sluijs & Brinkhuis, 2009) suggests that the mid-Atlantic Coastal Plain was a tropical river-dominated shelf during the PETM. In fact, the PETM mid-Atlantic Coastal Plain has been referred to as the “Appalachian Amazon” due to similarities with

sediments from the modern Amazon shelf, including features indicative of hyperpycnal flow (Self-Trail *et al.,* 2017), and the presence of kaolinitic clay (Gibson *et al.,* 2000) and magnetofossils (see Kopp *et al.,* 2009 and references therein).

Interestingly, present-day observations of two Amazon tributaries show a preferential loss of disordered carbon and an associated relative increase in graphite downstream (Bouchez *et al.,* 2010). The river is mostly supplied by low-grade metamorphic rocks from the Andes that are subject to a long residence time within the extensive meandering rivers of Amazon's large catchment. This results in the oxidation of the less recalcitrant OC_{petro} and an estimated loss of up to ~90 % of OC_{petro} during transport (Bouchez *et al.,* 2010; see Dellinger *et al.,* 2023 and references therein). The progressive shift towards more graphitised OC_{petro} along the land-to-sea transect is also seen in modern river systems with a contribution of high-grade metamorphic rocks, such as in the Himalayan catchment (Beyssac *et al.,* 2004). In the PETM mid-Atlantic Coastal Plain, the palaeo-Potomac river may have sourced high-grade graphite-rich rocks from the Appalachian Mountains. Concurrent with the exhumation and mobilisation of the Raritan Formation, this could explain the increase in percentage of graphitised OC_{petro} at SDB. However, the Himalayan catchment has a more efficient sediment routing system that also promotes burial of the less recalcitrant OC_{petro} in the Bengal Fan (Galy *et al.,* 2007). With the modern Amazon shelf as the closest analogue for the PETM mid-Atlantic Coastal Plain, we argue that most of the increase in percentage of graphitised carbon at SDB is due to the loss of disordered OC_{petro}.

Overall, the loss of disordered carbon likely indicates that there was enhanced oxidation of OC_{petro} in the PETM interval. If the mid-Atlantic Coastal Plain is representative of other localities, then the global estimate of OC_{petro}-derived CO_2 during the PETM is likely on the upper range of 10^4 PgC (Lyons *et al.,* 2019). However, evidence from other sites (ACEX; Fig. 3c) demonstrates that the response is spatially complex (Hollingsworth *et al.,* 2024). As the percentage of graphitised carbon did not increase during the POE, OC_{petro} oxidation may have had a less important role in modulating CO_2 in this interval. Multiple sites in the Atlantic Coastal Plain contain the POE, and reveal that it is a smaller-scale carbon cycle and climate aberration than compared to the onset of the PETM (see Babila *et al.,* 2022 and references therein). Future work should focus on understanding the other abiotic (*e.g.,* rainfall type, temperature, O_2 availability, mineral association) and biotic (*e.g.,* microbial activity) parameters that influence oxidation efficiencies (*e.g.,* see Hilton & West, 2020 and references

therein). Taken together, this study exemplifies that Raman spectroscopy is a useful tool that can both fingerprint OC_{petro} delivery and better determine OC_{petro} oxidation during the geological past.

Acknowledgements

E.H. Hollingsworth acknowledges funding from NERC (Grant NE/S007210). G.N. Inglis is supported by a GCRF Royal Society Dorothy Hodgkin Fellowship (DHF\R1\191178) with additional support via the Royal Society (RF\ERE\231019, RF\ERE\210068). This research used samples provided by the U.S. Geological Survey (USGS) and the International Ocean Drilling Program (IODP). We are grateful to Hayley Andrews from the Manchester Metropolitan University (MMU) for support with Raman spectroscopy. We thank Bart van Dongen for initiating this collaboration at the 2023 British Organic Geochemistry Meeting (BOGS).

Data Availability Statement

All the new data in this study are available in the Supporting Information.

References

Babila, T. L., Penman, D. E., Standish, C. D., Doubrawa, M., Bralower, T. J., Robinson, M. M., Self-Trail, J. M., Speijer, R. P., Stassen, P., Foster, G. L., & Zachos, J. C. (2022). Surface ocean warming and acidification driven by rapid carbon release precedes Paleocene-Eocene Thermal Maximum. *Science Advances*, *8*. https://doi.org/10.1126/sciadv.abg1025

Beyssac, O., Bollinger, L., Avouac, J. P., & Goffé, B. (2004). Thermal metamorphism in the lesser Himalaya of Nepal determined from Raman spectroscopy of carbonaceous material. *Earth and Planetary Science Letters*, *225*, 233–241. https://doi.org/10.1016/j.epsl.2004.05.023

Beyssac, O., Goffé, B., Chopin, C., & Rouzaud, J. N. (2002). Raman spectra of carbonaceous material in metasediments: A new geothermometer. *Journal of Metamorphic Geology*, *20*, 859–871. https://doi.org/10.1046/j.1525-1314.2002.00408.x

Bouchez, J., Beyssac, O., Galy, V., Gaillardet, J., France-lanord, C., Maurice, L., & Moreira-turcq, P. (2010). Oxidation of petrogenic organic carbon in the Amazon floodplain as a source of atmospheric CO2. *Geology*, *38*(3), 255–258. https://doi.org/10.1130/G30608.1

Bowen, G. J. (2013). Up in smoke: A role for organic carbon feedbacks in Paleogene

hyperthermals. *Global and Planetary Change*, *109*, 18–29. https://doi.org/10.1016/j.gloplacha.2013.07.001

Carmichael, M. J., Inglis, G. N., Badger, M. P. S., Naafs, B. D. A., Behrooz, L., Remmelzwaal, S., Monteiro, F. M., Rohrssen, M., Farnsworth, A., Buss, H. L., Dickson, A. J., Valdes, P. J., Lunt, D. J., & Pancost, R. D. (2017). Hydrological and associated biogeochemical consequences of rapid global warming during the Paleocene-Eocene Thermal Maximum. *Global and Planetary Change*, *157*, 114–138. https://doi.org/10.1016/j.gloplacha.2017.07.014

Dellinger, M., Hilton, R. G., Baronas, J. J., Torres, M. A., Burt, E. I., Clark, K. E., Galy, V., Ccahuana Quispe, A. J., & West, A. J. (2023). High rates of rock organic carbon oxidation sustained as Andean sediment transits the Amazon foreland- floodplain. *Proceedings of the National Academy of Sciences*, *120*(39). https://doi.org/10.1073/pnas

Galy, V., Beyssac, O., France-Lanord, C., & Eglinton, T. (2008). Recycling of Graphite During Himalayan Erosion: A Geological Stabilization of Carbon in the Crust. *Science*, *322*(5903), 943–945. https://doi.org/10.1126/science.1161408

Galy, V., France-Lanord, C., Beyssac, O., Faure, P., Kudrass, H., & Palhol, F. (2007). Efficient organic carbon burial in the Bengal fan sustained by the Himalayan erosional system. *Nature*, *450*(7168), 407–410. https://doi.org/10.1038/nature06273

Gibson, T. G., Bybell, L. M., & Mason, D. B. (2000). Stratigraphic and climatic implications of clay mineral changes around the Paleocene/Eocene boundary of the northeastern US margin. *Sedimentary Geology*, *134*(1–2), 65–92. https://doi.org/10.1016/S0037-0738(00)00014-2

Hilton, R. G., Gaillardet, J., Calmels, D., & Birck, J. (2014). Geological respiration of a mountain belt revealed by the trace element rhenium. *Earth and Planetary Science Letters*, *403*, 27–36. https://doi.org/10.1016/j.epsl.2014.06.021

Hilton, R. G., & West, A. J. (2020). Mountains, erosion and the carbon cycle. *Nature Reviews Earth & Environment*, *1*, 284–299. https://doi.org/10.1038/s43017-020-0058-6

Hollingsworth, E. H., Elling, F. J., Badger, M. P. S., Pancost, R. D., Dickson, A. J., Rees-Owen, R. L., Papadomanolaki, N. M., Pearson, A., Sluijs, A., Freeman, K. H., Baczynski, A. A., Foster, G. L., Whiteside, J. H., & Inglis, G. N. (2024). Spatial and Temporal Patterns in Petrogenic Organic Carbon Mobilization During the Paleocene-Eocene Thermal Maximum. *Paleoceanography and Paleoclimatology*, *39*. https://doi.org/10.1029/2023PA004773

Hollis, C. J., Dunkley Jones, T., Anagnostou, E., Bijl, P. K., Cramwinckel, M. J., Cui, Y.,

Dickens, G. R., Edgar, K. M., Eley, Y., Evans, D., Foster, G. L., Frieling, J., Inglis, G. N., Kennedy, E. M., Kozdon, R., Lauretano, V., Lear, C. H., Littler, K., Lourens, L., … Lunt, D. J. (2019). The DeepMIP contribution to PMIP4: Methodologies for selection, compilation and analysis of latest Paleocene and early Eocene climate proxy data, incorporating version 0.1 of the DeepMIP database. *Geoscientific Model Development*, *12*(7), 3149–3206. https://doi.org/10.5194/gmd-12-3149-2019

Jehlicka, J., & Rouzaud, J.-N. (1990). Organic geochemistry of precambrian shales and schists (Bohemian massif, Central Europe). *Organic Geochemistry*, *16*(4–6), 865–872. https://doi.org/10.1016/0146-6380(90)90123-H

Jin, S., Kemp, D. B., Shen, J., Yin, R., Jolley, D. W., Vieira, M., & Huang, C. (2024). Spatiotemporal distribution of global mercury enrichments through the Paleocene-Eocene Thermal Maximum and links to volcanism. *Earth-Science Reviews*, *248*. https://doi.org/10.1016/j.earscirev.2023.104647

John, C. M., Bohaty, S. M., Zachos, J. C., Sluijs, A., Gibbs, S., Brinkhuis, H., & Bralower, T. J. (2008). North American continental margin records of the Paleocene-Eocene thermal maximum: Implications for global carbon and hydrological cycling. *Paleoceanography*, *23*(2), 1–20. https://doi.org/10.1029/2007PA001465

Kirtland Turner, S. (2018). Constraints on the onset duration of the Paleocene-Eocene Thermal Maximum. *Philosophical Transactions of the Royal Society A*, *376*(2130), 1–16. https://doi.org/10.1098/rsta.2017.0082

Kopp, R. E., Schumann, D., Raub, T. D., Powars, D. S., Godfrey, L. V., Swanson-Hysell, N. L., Maloof, A. C., & Vali, H. (2009). An Appalachian Amazon? Magnetofossil evidence for the development of a tropical river-like system in the mid-Atlantic United States during the Paleocene-Eocene thermal maximum. *Paleoceanography*, *24*(4), 1–17. https://doi.org/10.1029/2009PA001783

Lyons, S. L., Baczynski, A. A., Babila, T. L., Bralower, T. J., Hajek, E. A., Kump, L. R., Polites, E. G., Self-Trail, J. M., Trampush, S. M., Vornlocher, J. R., Zachos, J. C., & Freeman, K. H. (2019). Palaeocene–Eocene Thermal Maximum prolonged by fossil carbon oxidation. *Nature Geoscience*, *12*, 54–60. https://doi.org/10.1038/s41561-018-0277-3

Self-Trail, J. M., Robinson, M. M., Bralower, T. J., Sessa, J. A., Hajek, E. A., Kump, L. R., Trampush, S. M., Willard, D. A., Edwards, L. E., Powars, D. S., & Wandless, G. A. (2017). Shallow marine response to global climate change during the Paleocene-Eocene Thermal Maximum, Salisbury Embayment, USA. *Paleoceanography*, *32*, 710–728.

https://doi.org/10.1002/2017PA003096

Sluijs, A., & Brinkhuis, H. (2009). A dynamic climate and ecosystem state during the Paleocene-Eocene Thermal Maximum: Inferences from dinoflagellate cyst assemblages on the New Jersey Shelf. *Biogeosciences*, *6*(8), 1755–1781. https://doi.org/10.5194/bg-6-1755-2009

Sluijs, A., Röhl, U., Schouten, S., Brumsack, H.-I., Sangiorgi, F., Sinninghe Damsté, J. S., & Brinkhuis, H. (2008). Arctic late Paleocene–early Eocene paleoenvironments with special emphasis on the Paleocene-Eocene thermal maximum (Lomonosov Ridge , Integrated Ocean Drilling Program Expedition 302). *Paleoceanography*, *23*(1), 1–17. https://doi.org/10.1029/2007PA001495

Sparkes, R. B., Hovius, N., Galy, A., & Liu, J. T. (2020). Survival of graphitized petrogenic organic carbon through multiple erosional cycles. *Earth and Planetary Science Letters*, *531*. https://doi.org/10.1016/j.epsl.2019.115992

Sparkes, R. B., Hovius, N., Galy, A., Vasant Kumar, R., & Liud, J. T. (2013). Automated analysis of carbon in powdered geological and environmental samples by Raman spectroscopy. *Applied Spectroscopy*, *67*(7), 779–788. https://doi.org/10.1366/12-06826

Sparkes, R. B., Maher, M., Blewett, J., Selver, A. O., Gustafsson, O., Semiletov, I. P., & Van Dongen, B. E. (2018). Carbonaceous material export from Siberian permafrost tracked across the Arctic Shelf using Raman spectroscopy. *Cryosphere*, *12*, 3293–3309. https://doi.org/10.5194/tc-12-3293-2018

Sun, X., Fan, D., Hu, L., Yang, Z., & Guo, Z. (2022). Oxidation of petrogenic organic carbon in a large river-dominated estuary. *Geochimica et Cosmochimica Acta*, *338*, 136–153. https://doi.org/10.1016/j.gca.2022.10.028

Tierney, J. E., Zhu, J., Li, M., Ridgwell, A., Hakim, G. J., Poulsen, C. J., Whiteford, R. D. M., Rae, J. W. B., & Kump, L. R. (2022). Spatial patterns of climate change across the Paleocene–Eocene Thermal Maximum. *Proceedings of the National Academy of Sciences of the United States of America*, *119*(42), 1–7. https://doi.org/10.1073/pnas.2205326119

Zeebe, R. E. (2013). What caused the long duration of the Paleocene-Eocene Thermal Maximum? *Paleoceanography*, *28*, 440–452. https://doi.org/10.1002/palo.20039

Zeebe, R. E., & Lourens, L. J. (2019). Solar System chaos and the Paleocene–Eocene boundary age constrained by geology and astronomy. *Science*, *929*(6456), 926–929. https://doi.org/10.1126/science.aax0612

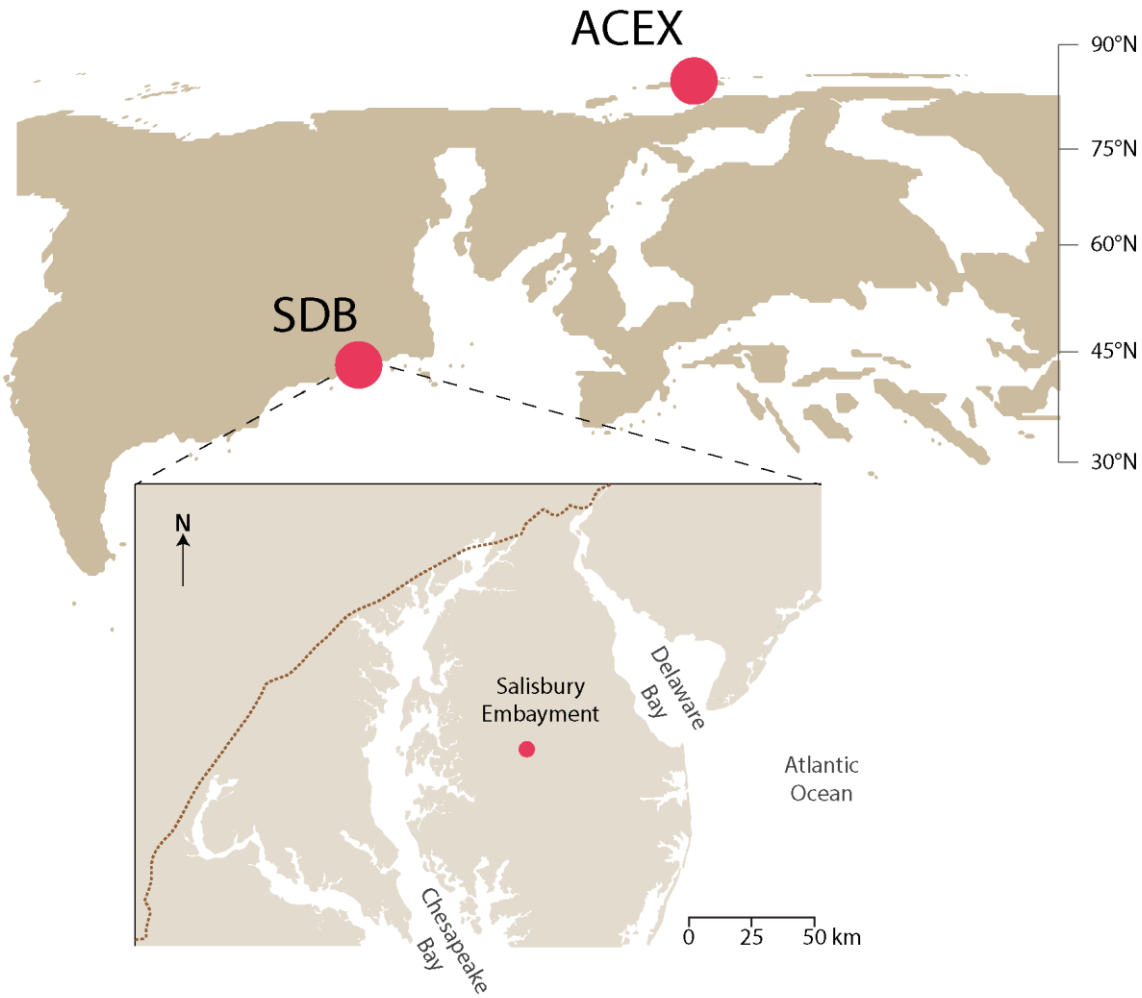

Figure 1 Location of the Arctic Coring Expedition (ACEX; 82.81°N, 66.91°E) and South Dover Bridge (SDB; 41.39°N, 59.48°W) during the Paleocene-Eocene Thermal Maximum (palaeo-latitudes based on mantle reference frame; Hollis *et al.*, 2019). The top map represents the palaeogeography of the Northern Hemisphere 56 Ma, adapted from Carmichael et al. (2017). The bottom map presents the mid-Atlantic Coastal Plain with the modern coastline and Fall Line (brown dashed line).

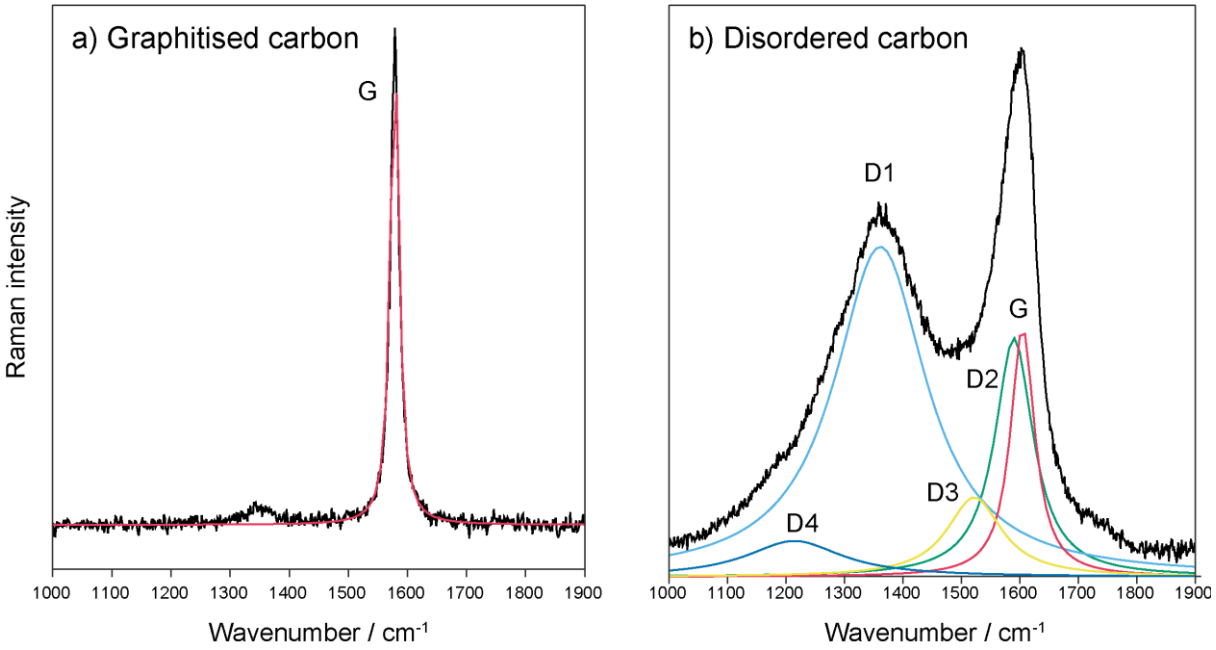

Figure 2 Example spectra (black) with fitted peaks (coloured) for **(a)** graphitised carbon, from a SDB sample at 200.28 m and **(b)** disordered carbon, from an ACEX sample at 385.11 mcd. The background is removed from the spectra during the automated fitting process and the fitted peaks include: G (1580 cm^{-1}), D1 (1350 cm^{-1}), D2 (1620 cm^{-1}), D3 (1500 cm^{-1}), and D4 (1200 cm^{-1}) (Sparkes *et al.*, 2013).

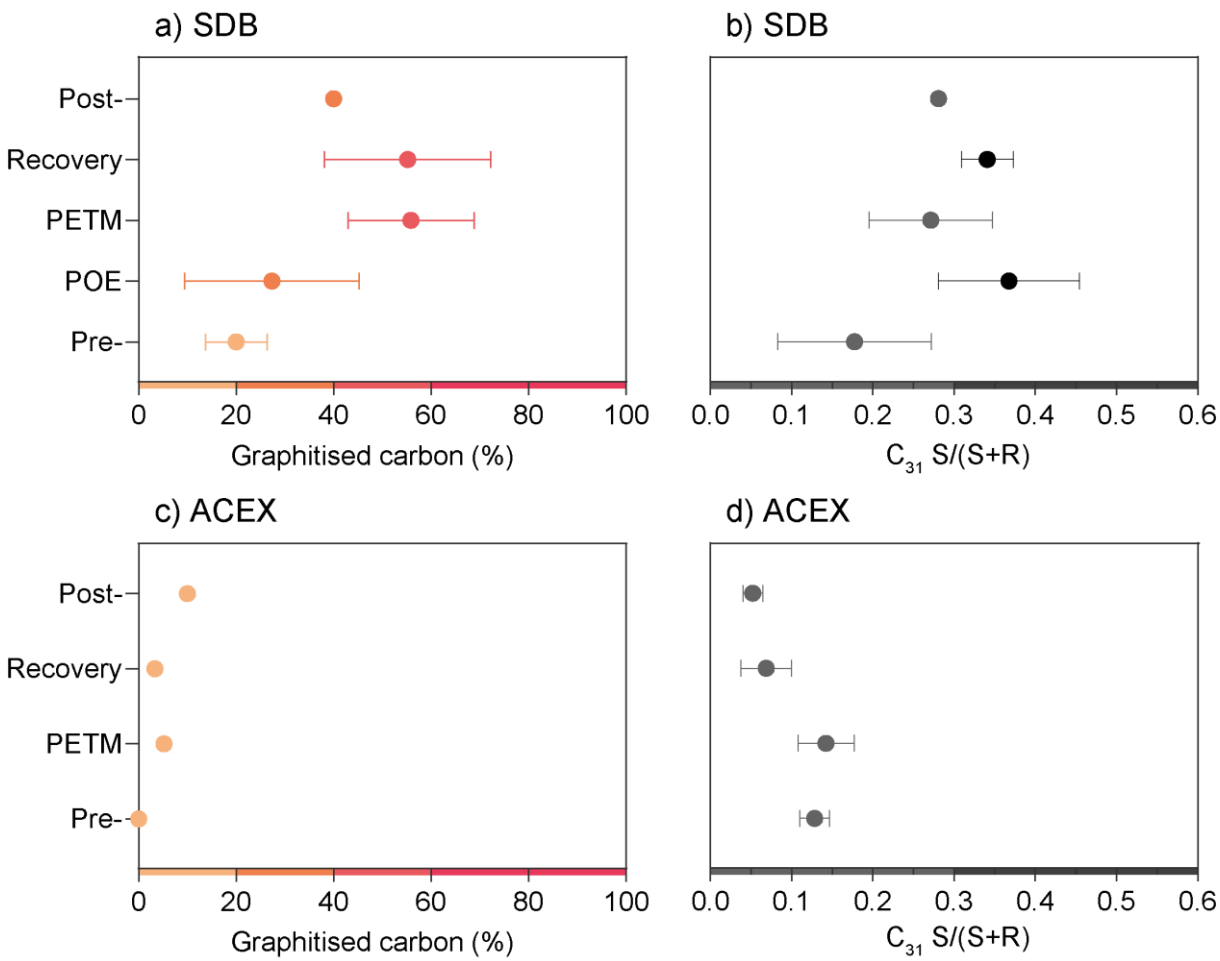

Figure 3 Mean percentages of graphitised carbon (this study) and mean values of the C_{31} S/(S+R) ratio (Lyons *et al.*, 2019; Hollingsworth *et al.*, 2024), from **(a–b)** SDB and **(c–d)** ACEX. The time intervals are as follows: Pre-PETM, PETM (onset and body), Recovery, and Post-PETM (see Hollingsworth *et al.*, 2024 and references therein). At SDB, the pre-onset excursion (POE) in the pre-PETM interval is isolated using the definition from Babila et al. (2022). The uncertainty is displayed as the 95 % confidence interval of the mean, with error bars not included when sample size is <4.

Supplementary Information

The Supplementary Information includes:

- Tables S-1 to S-2
- Figures S-1 to S-2
- Supplementary Information References

Table S-1 Number of disordered carbon vs. graphitised carbon spectra from SDB, with duplicate results in parenthesis*. The time intervals are as follows: Pre-PETM, PETM (onset/body), Recovery, and Post-PETM, based on Hollingsworth et al. (2024) and references therein. The Pre-onset Excursion (POE) in the pre-PETM interval is isolated using the definition from Babila et al. (2022).

Time interval	**Approx. sample depth (m)**	**Disordered carbon**	**Graphitised carbon**
Post-PETM	186.6	5	5
Post-PETM	188	7	3
Recovery	190.99	6	3
Recovery	192.57	5	5
Recovery	193.3	5	5
Recovery	193.88	2	7
Recovery	195.07	5	5
Recovery	196.41	3	7
PETM	196.93	3	7
PETM	197.21	2 (4)	8 (6)
PETM	199.52	3	7
PETM	199.83	4	6
PETM	200.28	2	8
PETM	200.83	2	7
PETM	201.47	3	6
PETM	202.08	3	7
PETM	202.37	4 (9)	6 (1)
PETM	202.68	7	3
PETM	202.98	5	4
PETM	203.06	7 (7)	3 (2)
PETM	203.3	6	3
PETM	203.88	9	1
Pre-PETM	204.26	9	1
Pre-PETM	204.49	8	2
Pre-PETM	204.84	8	2
Pre-PETM	205.12	9 (9)	1 (1)

Pre-PETM	205.4	8	2
Pre-PETM	205.44	8	2
Pre-PETM	205.74	7	3
POE	206.04	8	2
POE	206.35	9	1
POE	206.41	5	4
POE	206.68	9	1
POE	207.04	5	5
POE	207.08	7	3
Pre-PETM	208.83	7	3

*In order to assess whether the semi-quantitative approach using 10 spectra per sample can accurately represent the population, duplicate analyses were undertaken on 4 samples from SDB. The differences in the results are not unexpected, considering the heterogenous nature of shallow-marine sediments and the relatively low maximum total organic carbon of 0.68 % and 4.86 % for SDB (Lyons et al., 2019) and ACEX (Elling et al., 2019), respectively. However, the largest variability appears to be restricted to the transition zone from dominantly disordered carbon to graphitised carbon (~202.37 m).

Table S-2 Number of disordered carbon vs. graphitised carbon spectra from ACEX. The time intervals are as follows: Pre-PETM, PETM (onset/body), Recovery, and Post-PETM, based on Hollingsworth et al. (2024) and references therein.

Time interval	**Depth (mcd)**	**Freeze-dried**	**Oven-dried**	**Disordered carbon**	**Graphitised carbon**
Post-PETM	378.14	Yes		9	1
Recovery	378.69		Yes	10	0
Recovery	380.73	Yes		10	0
Recovery	381.56	Yes		9	1
PETM	382.15		Yes	9	1
PETM	382.94		Yes	8	1
PETM	383.87		Yes	10	0
PETM	385.11		Yes	10	0
Pre-PETM	388.03		Yes	10	0
Pre-PETM	388.87	Yes		10	0
Pre-PETM	389.75		Yes	10	0
Pre-PETM	390.78	Yes		10	0

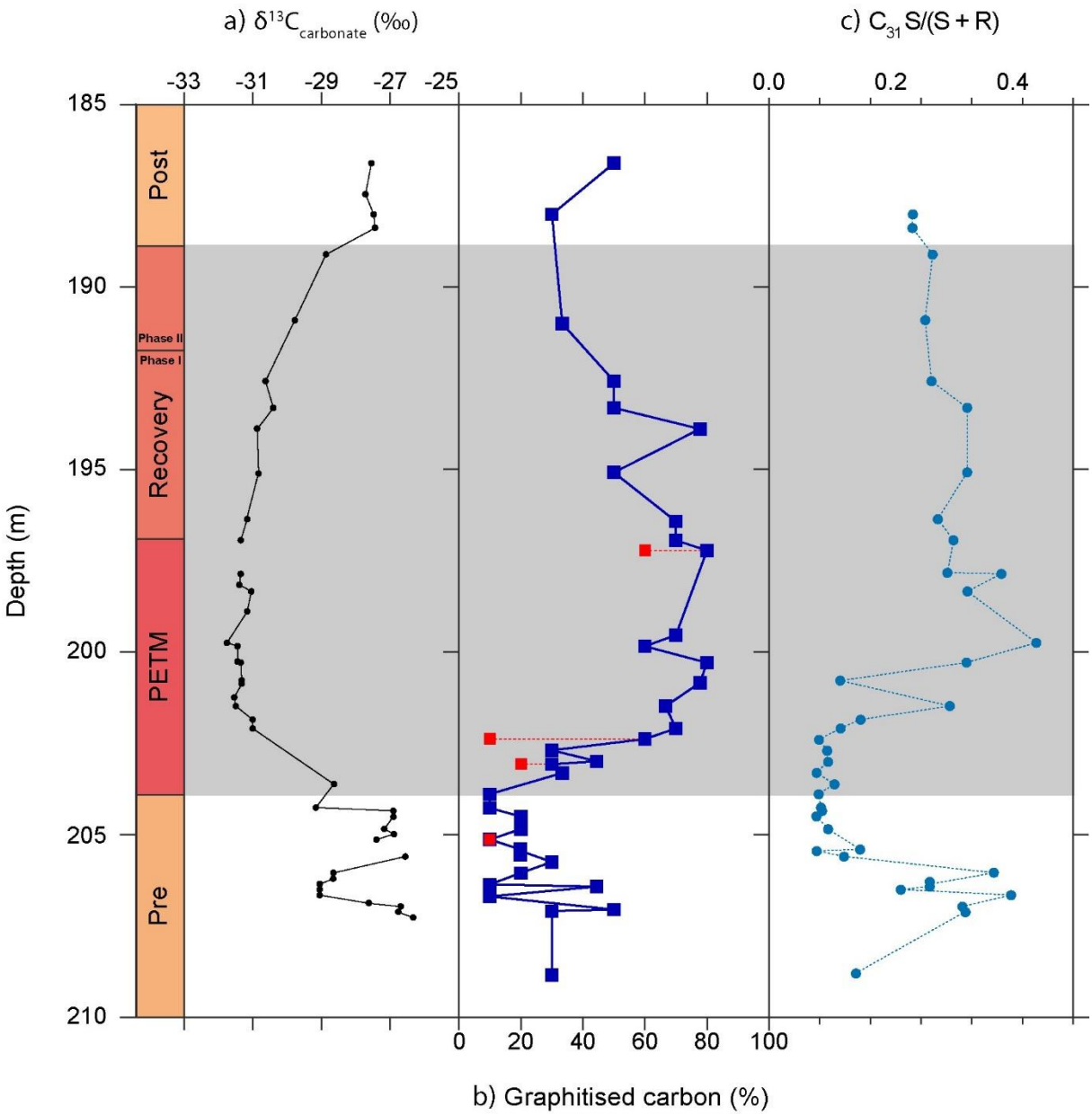

Figure S-1 The SDB record of **(a)** bulk sediment $\delta^{13}C$ of carbonates ($\delta^{13}C_{carbonates}$; Lyons et al., 2019) **(b)** percentage graphitised carbon (this study) **(c)** C_{31} S/(S + R) ratio (Lyons et al., 2019). The red symbols within panel **(b)** are duplicate measurements done on samples that represent: low percentage graphitised carbon (10%), the transition zone (30–60%), and high percentage graphitised carbon (80%). The duplicate measurement on 203.06 m consists of 9 spectra, as 1 spectrum was excluded due to a noise-to-signal ratio greater than 1:3. The time intervals are as follows: Pre-PETM, PETM (onset/body), Recovery Phase I, Recovery Phase II, and Post-PETM, based on Hollingsworth et al., (2024) and references therein.

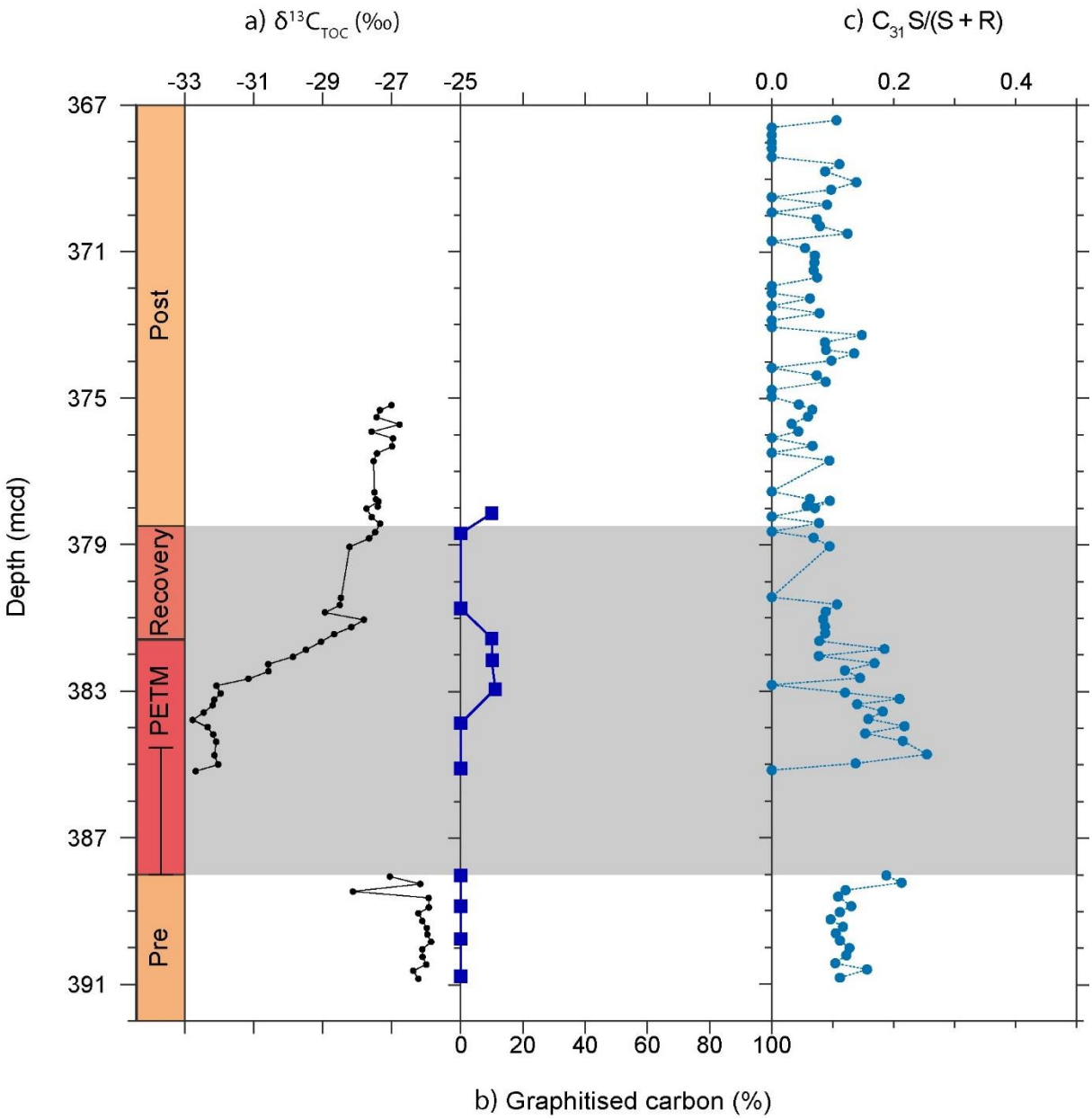

Figure S-2 The ACEX record of **(a)** bulk sediment $\delta^{13}C$ of total organic carbon ($\delta^{13}C_{TOC}$; Elling et al., 2019) **(b)** percentage graphitised carbon (this study) **(c)** C_{31} S/(S + R) ratio (Hollingsworth et al., 2024). The time intervals are as follows: Pre-PETM, PETM (onset/body), Recovery, and Post-PETM, based on Hollingsworth et al. (2024) and references therein. Note the core gap from ~388–384.5 mcd (Sluijs et al., 2006).

Supplementary Information References

Babila, T. L., Penman, D. E., Standish, C. D., Doubrawa, M., Bralower, T. J., Robinson, M. M., Self-Trail, J. M., Speijer, R. P., Stassen, P., Foster, G. L., & Zachos, J. C. (2022). Surface ocean warming and acidification driven by rapid carbon release precedes Paleocene-Eocene Thermal Maximum. *Science Advances*, *8*. https://doi.org/10.1126/sciadv.abg1025

Elling, F. J., Gottschalk, J., Doeana, K. D., Kusch, S., Hurley, S. J., & Pearson, A. (2019). Archaeal lipid biomarker constraints on the Paleocene-Eocene carbon isotope excursion. *Nature Communications*, *10*(1), 1–10. https://doi.org/10.1038/s41467-019-12553-3

Hollingsworth, E. H., Elling, F. J., Badger, M. P. S., Pancost, R. D., Dickson, A. J., Rees-Owen, R. L., Papadomanolaki, N. M., Pearson, A., Sluijs, A., Freeman, K. H., Baczynski, A. A., Foster, G. L., Whiteside, J. H., & Inglis, G. N. (2024). Spatial and Temporal Patterns in Petrogenic Organic Carbon Mobilization During the Paleocene-Eocene Thermal Maximum. *Paleoceanography and Paleoclimatology*, *39*. https://doi.org/10.1029/2023PA004773

Lyons, S. L., Baczynski, A. A., Babila, T. L., Bralower, T. J., Hajek, E. A., Kump, L. R., Polites, E. G., Self-Trail, J. M., Trampush, S. M., Vornlocher, J. R., Zachos, J. C., & Freeman, K. H. (2019). Palaeocene–Eocene Thermal Maximum prolonged by fossil carbon oxidation. *Nature Geoscience*, *12*, 54–60. https://doi.org/10.1038/s41561-018-0277-3

Sluijs, A., Schouten, S., Pagani, M., Woltering, M., Brinkhuis, H., Dickens, G. R., Huber, M., Reichart, G., Stein, R., Matthiessen, J., Lourens, L. J., Pedentchouk, N., Backman, J., & Moran, K. (2006). Subtropical Arctic Ocean temperatures during the Palaeocene/Eocene thermal maximum. *Nature*, *441*(1), 610–613. https://doi.org/10.1038/nature04668